Supporting Information for

Formation and Healing of Defects in Atomically Thin GaSe & InSe

David G. Hopkinson[1,2], Viktor Zólyomi[1,3], Aidan P. Rooney[2†], Nick Clark[1,2], Daniel J. Terry[1,3], Matthew Hamer[1,3], David J. Lewis[2], Christopher S. Allen[4,5], Angus I. Kirkland[4,5], Yuri Andreev[6], Zakhar Kudrynskyi[7], Zakhar Kovalyuk[8], Amalia Patanè[7], Vladimir I. Fal'ko[1,3], Roman Gorbachev[1,3], Sarah J. Haigh[1,2*]*

1. National Graphene Institute, University of Manchester, Booth Street East, M13 9PL, United Kingdom

2. School of Materials, University of Manchester, Oxford Road, Manchester, M13 9PL, United Kingdom

3. School of Physics and Astronomy, University of Manchester, Oxford Road, M13 9PL, United Kingdom

4. Electron Physical Sciences Imaging Centre, Diamond Light Source Ltd., Didcot, Oxfordshire, OX11 0DE, United Kingdom

5. Department of Materials, University of Oxford, Parks Road, Oxford, OX1 3PH, United Kingdom

6. National Tomsk State University, 634050 Tomsk, Russian Federation

7. School of Physics and Astronomy, University of Nottingham, Nottingham, NG7 2RD, United Kingdom

8. Institute for Problems of Materials Science, National Academy of Sciences of Ukraine, Chernivtsi Branch, 58001 Chernivtsi, Ukraine

* roman@manchester.ac.uk; sarah.haigh@manchester.ac.uk

Contents

1. Defect Formation Energy, E_F

Defect formation energy, E_F, was defined by the difference in total energy between the defective supercell (E_{Vac}) and free atom (E_{Atom}), and the defect-free supercell ($E_{Perfect\ Lattice}$):

$$E_F = (E_{Vacancy} + E_{Atom}) - E_{Perfect\ Lattice}$$

Defect pairs were likewise defined by the difference in total energies as follows:

$$E_F = (E_{V_1 + V_2} + E_{A_1} + E_{A_2}) - E_{Perfect\ Lattice}$$

Negative formation energies indicate the resultant structure is more energetically favorable than the initial structure. The calculated formation energies are presented in tabulated form below.

	E_F (eV)	
	GaSe	InSe
V_M	6.360	5.615
V_{Se}	6.707	6.178
$V_M + V_{Se}$	12.038	10.932
$V_{Se} + V_{Se}$	13.415	12.373
O_{Se}	-3.030	-2.616

Table S1 – Relaxed defect formation energies E_F and E_F'.

Additionally, the formation energies for defects adjacent to pre-existing defects were defined by the energy difference between the formation energies (c.f. total energy) of the supercell with the defect pair, and the supercell containing the single defect (derivation available from the authors on request):

$$E_F\ (V_2\ @\ V_1) = E_F\ (V_1 + V_2) - E_F\ (V_1)$$

2. Elastic Displacement Cross-Section, σ_D

The elastic displacement cross-section, σ_D, was calculated from code written by Eder & Kotakoski and provided in the erratum[1] to a paper by Meyer *et al*[2] This utilized McKinley & Feshbach's analytic expression[3] of the Mott scattering cross-section[4] with temperature (phonon) effects incorporated by a Debye model. The key input parameters are atomic mass, atomic number, temperature, displacement threshold energy (E_{thr}), and Debye temperature (T_D). These were used to calculate scattering cross-section as a function of incident electron energy/beam energy.

The atomic mass and number for Ga, In, and Se were obtained from standard sources, and a nominal temperature of 300 K was used, approximating imaging conditions at room temperature.

Komsa *et al*,[5] have demonstrated that, for transition metal dichalcogenides, the displacement threshold energy calculated *via* DFT MD closely correlates with the corresponding defect formation energy for an unrelaxed system (this relationship breaks down for relaxed structures due to the energy minimisation). As such, in this work, the defect formation energies for structures prior to

relaxation (E^*_F) were used as a close approximation to E_{thr} *in lieu* of separately calculated threshold energies. These values are given in Table S2:

	E^*_F (eV)	
	GaSe	InSe
V_M	7.638	7.475
V_{Se}	7.262	6.761
V_M @ V_{Se}	6.051	5.851
V_{Se} @ V_M	5.675	5.137
V_{Se} @ V_{Se}	7.262	6.761

Table S2 – Unrelaxed defect formation energy/displacement threshold
energy for the four different single vacancy types and their variants.

Literature Debye temperatures, T_D, for elemental Ga (T_D = 240 K), In (T_D = 129 K), and Se (T_D = 150 K) were obtained from Ho, Powell, & Liley.[6]

We note that the literature values of T_D for Ga and In are at T = 298 K, whilst T_D used for Se is at T < 298 K, as room temperature measurements of T_D for Se are not available. However, this is unlikely to dramatically affect the σ_D plot and the validity of the conclusions made in the main text, as Meyer *et al*[2] have already shown that cross-sections incorporating the Debye model at 0 K and 300 K were almost identical. This was concluded to be due to the zero-point energy of the phonon modes being sufficient to describe the gradual increase in scattering cross-section, relative to the static lattice. The results of these calculations are shown in Figure S4.

3. Maximum Energy Transfer, E_{max}

The calculation method for determining the maximum energy transfer from an electron-atomic nucleus collision (the cause of elastic knock-on and sputtering damage) was taken from Garcia *et al*[7] The relevant equation incorporating relativistic kinematics is given by:

$$E_{max} = \frac{E_{beam}(E_{beam} + 2m_e c^2)}{E_{beam} + \frac{\left(1 + \frac{m_e}{M}\right)^2 Mc^2}{2}}$$

Where E_{max} is maximum energy transfer, E_{beam} is incident electron beam energy, m_e is the electron rest mass, c is the speed of light, and M is the atomic mass of the target nucleus.

Calculations were implemented in Python and executed for Ga (M = 69.723 u), In (M = 114.82 u), and Se (M = 78.96 u) for beam energies ranging 1-300 keV, at increments of 1 keV (Figure S5).

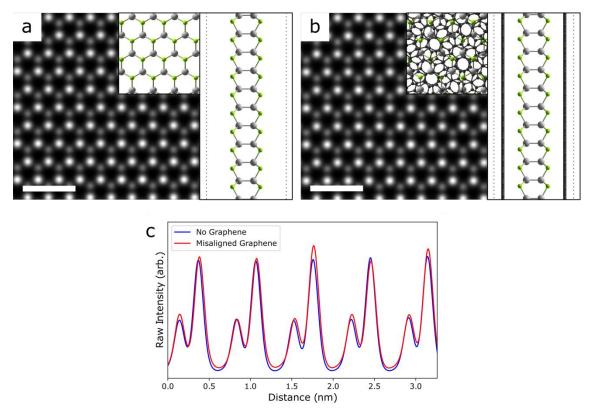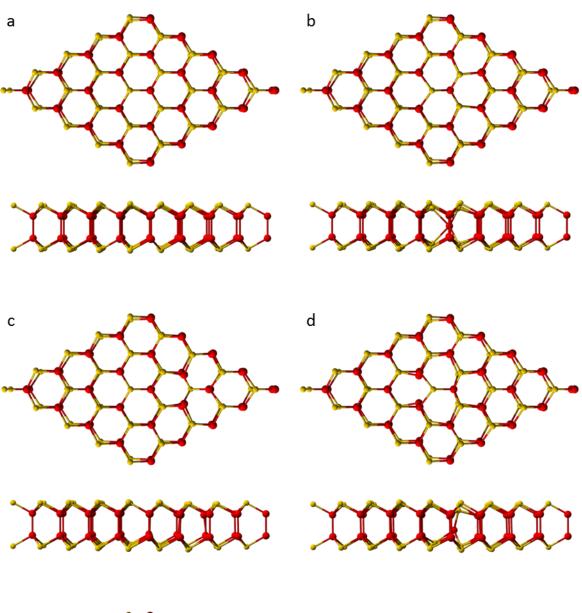## 4. Influence of Graphene Encapsulation on ADF Intensity

Figure S1 – **Multislice ADF image simulations with and without graphene encapsulation.** (a) Image simulation of monolayer InSe, with structural model in plan view (inset) and side view (right). (b) Image simulation of monolayer InSe with randomly orientated monolayer graphene encapsulation with structural model in plan view (inset) and side view (right). Carbon atoms are shown in dark gray. All scale bars: 1 nm. (c) Comparison of raw intensity profiles for graphene encapsulated and unencapsulated monolayer InSe. The effect of graphene on intensity is minimal.
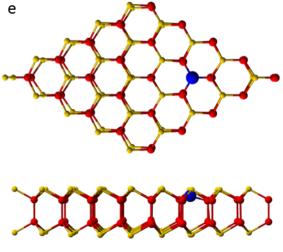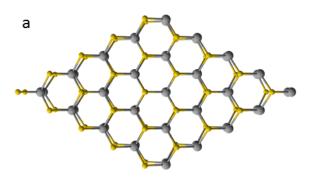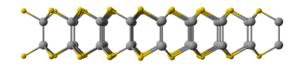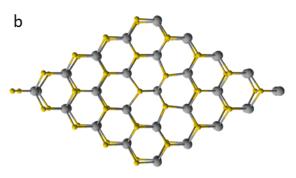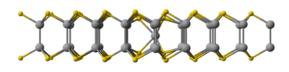
5. DFT Relaxed Crystal Models

Figure S2 – **Relaxed 5x5 supercell of defective GaSe.** (a) Defect free. (b) V_{Ga}. (c) VSe. (d) V_{Ga} + V_{Se}. (e) O_{Se}. For all models, the upper image is viewed along [001] and the lower along [110]. Red atoms are gallium, orange are selenium, and blue are oxygen.
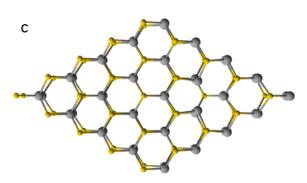
Figure S3 – **Relaxed 5x5 supercell of defective InSe.** (a) Defect free. (b) V_{In}. (c) VSe. (d) V_{In} + V_{Se}. (e) O_{Se}. For all models, the upper image is viewed along [001] and the lower along [110]. Grey atoms are indium, orange are selenium, and blue are oxygen.
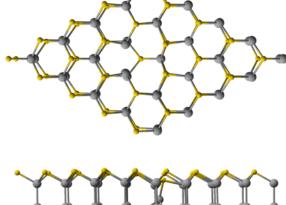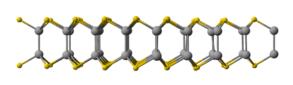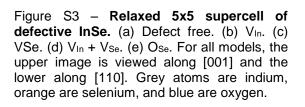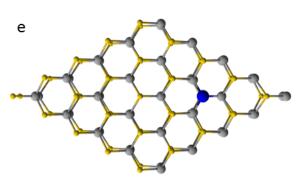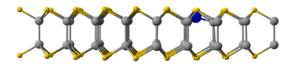
6. Beam Induced Defect Formation Mechanism

To differentiate the nature of the beam-induced defect formation mechanisms as either elastic (incident electron interacting with the atomic nucleus with no energy transfer) or inelastic (incident electron interacting with the electron cloud with energy transfer), the elastic Mott scattering cross-sections and the maximum energy transfer from an incident electron to a target Ga, In, or Se atom were calculated following the methods described by Meyer *et al*,[2] and Garcia *et al*,[7] respectively. As shown in Figure S4, at an electron beam energy of 80 keV, the elastic Mott scattering cross section is very small for all native atom species in these crystals. In addition, the maximum energy transferred by the beam (Figure S5) is insufficient to exceed the displacement threshold energy for any of the elements both in the pristine crystal and at defect sites. It can thus be concluded that elastic damage mechanisms, such as knock-on or sputtering, are unlikely to dominate under these conditions and so
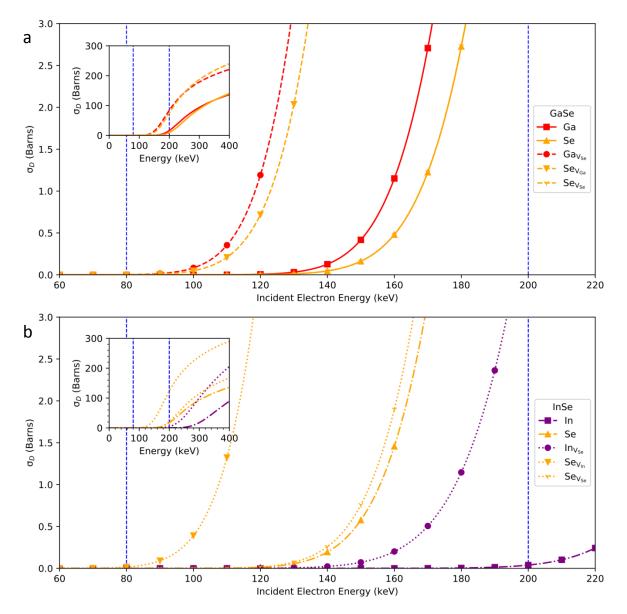

Figure S4 – **Elastic scattering cross sections for atoms in GaSe and InSe.** Cross-sections for atoms in GaSe (a) and InSe (b) ranging 60-220 keV. Inset in both is an overview for the total calculated energy ranging 0-400 keV.
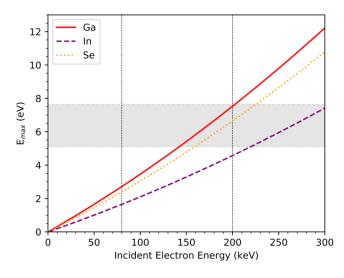
Figure S5 – **Maximum elastic energy transfer to atoms of gallium, indium, and selenium from electrons with energies ranging 0-300 keV.**

are highly unlikely to be the cause of the damage reported in this work.

In an attempt to understand the formation of these extended defects we have computed an approximate barrier height for the diffusion of chalcogen vacancies in the limit of strictly lateral diffusion along a straight line connecting the vacancy and the nearest chalcogen lattice site that it can leap to. Within an accuracy of 1 meV this value is the same in GaSe and InSe (12 meV) which leads us to expect that the height of the barrier is comparable between the two materials. However, a full computation consideration of the barrier heights for defect diffusion is difficult due to the large supercell sizes involved in the calculations. This is beyond the scope of this work but is an interesting area for future studies.

7. EELS data analysis

Particular care was required to extract the elemental maps from the electron energy loss spectrum images due to the possibility of the $InM_{4,5}$ (443 eV) peak overlapping with the OK (532 eV edge). Low loss (eV) and core loss (eV) EEL spectra were simultaneously acquired in Dual EELS mode which allowed simultaneous acquisition of the carbon K edge (284 eV), oxygen K edge (532 eV), and the indium $M_{4,5}$ edge (443 eV). To process this data, each 'equal energy slice' was first median filtered (nearest neighbour kernel) to remove high intensity spikes due to X-rays. Low loss and core loss spectra were aligned to compensate for spectral drift using the zero loss peak in the low loss spectra. Dimensionality reduction using singular value decomposition (SVD) with 9 components was then performed on the core loss spectra to increase the signal to noise ratio.

Figure S6 shows raw spectra (dots in S6b and c) from 3 points from the InSe spectral map (S6a) used in the paper (averaged over 2x2 pixels), compared to the SVD rebuilt spectra (solid lines). The oxygen K edge is clearly visible in the red and blue spectra at 532 eV. A large In M edge is also seen in the red spectra at 443 eV. Individual edge strengths were then extracted using model based fitting. The carbon edge was fitted separately from the In and O edges to reduce processing time. The In / O

spectra was fit to a model with 4 components, representing the In M_4, In M_5, O K edges and a power law background component. Results of the fitting process for the same three spectra presented in Figure S6 shown in Figure S7. Here, single pixel data is shown (as opposed to 2x2 rebinned data as in Figure S6). The 3 components (In $M_{4,5}$ are combined here for simplicity) obtained from the fit to the SVD rebuilt spectra are also shown.

To confirm we have not been too aggressive denoising the spectra during dimensionality reduction, we also present resultant maps from the fitting process described previously performed on the original spectra (rebinned by 4 in energy) in Figure S8 alongside those obtained from the SVD rebuilt spectra. Both the maps and profiles are quantitatively very similar.
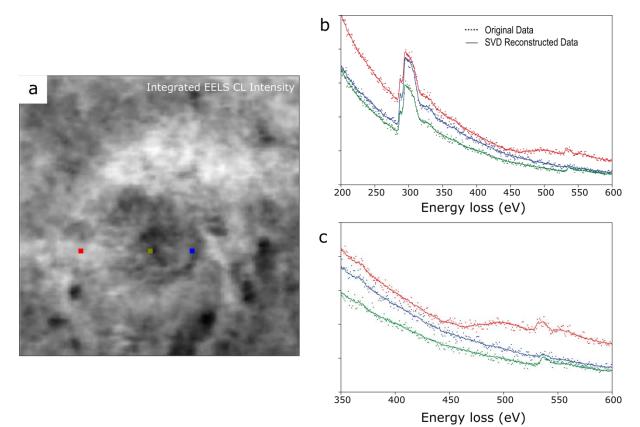

Figure S6 – **Core loss EEL spectra from 3 regions from spectrum image presented as In and O maps in the main text.** (a) Energy integrated core loss map, along with the locations of the 3 spectra, marked by colored squares. The spectra are averaged over a 2x2 pixel region. The dots represent the raw data (also binned by 4 in the energy dimension to increase the signal-to-noise ratio). The solid lines show rebuilt spectra after SVD dimensionality reduction with 9 components. The blue spectra show little evidence of In (443 eV) or O (532 eV). The green spectra show a significant oxygen peak, but no sign of indium. The red spectra clearly show an $In_{M4,5}$ edge starting at 443 eV as well as an O_K edge at 532 eV. All 3 show a clear C_K edge (284 eV).
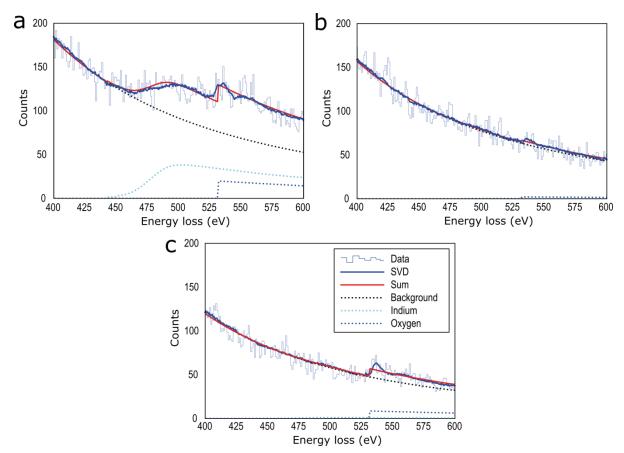
Figure S7 – **Model based fitting of EEL spectra.** Fitting results for spectra from the 3 regions ((a) red, (b) blue, and (c) green) in Figure S6. In this case the raw data has not been rebinned, so the noise level from the raw data (steps) is higher than Figure S6. The model components (dotted lines) were fit to the SVD rebuilt spectra (solid blue line).
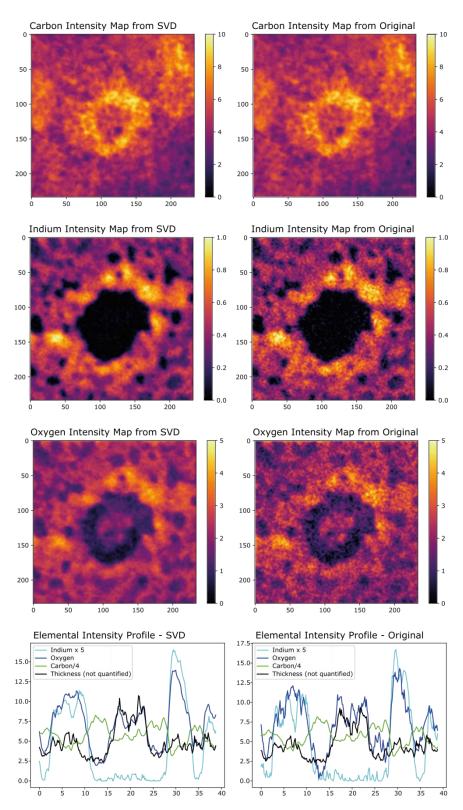
Figure S8 – **Comparison of model based fitting raw data (right) rather than SVD rebuilt data (left).** Left-hand side maps and profiles are those presented in the main paper, and right-hand side maps are those generated by directly fitting to the raw data. The maps are qualitatively extremely similar for all elements but the O and In benefit from improved signal to noise with the SVD rebuilt data. Horizontal profiles (lower panel) show the elemental composition half way down the vertical spatial axis.
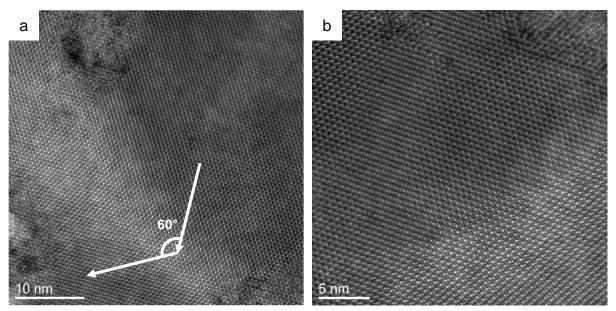
12

8. Stacking Faults in Few-Layer InSe

Figure S9 – **Stacking faults in bilayer InSe.** (a) Larger field-of-view image of the stacking fault as shown in Figure 8h in the main text with shear directions indicated by arrows. (b) Multiple stacking faults near to a crack edge (located towards the top right of the image).

9. ADF Intensity Analysis of Stacking Sequences in Bilayer GaSe and InSe

In order to determine the stacking sequences present in bilayer GaSe and InSe, ADF simulations
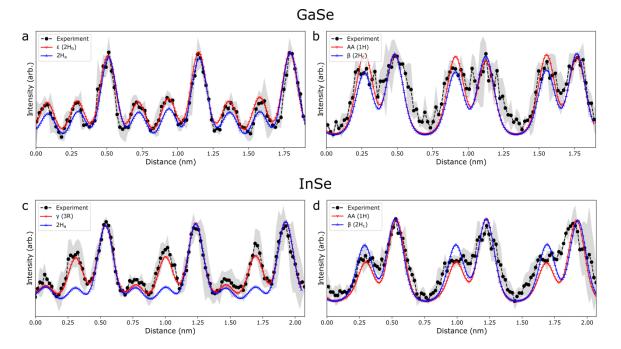

Figure S10 – **Stacking sequence determination through ADF analysis.** (a, c) Line profiles of the experimental ADF intensity for regions indicated in Figure 8b and 8r for GaSe and InSe, respectively demonstrating a good fit to the expected stable polytypes of ε and γ respectively (these polytypes were also identified from diffraction analysis). (b, d) Line profiles of the experimental ADF intensity for stacking fault regions indicated in Figure 8h and 8l for GaSe and InSe, respectively. The experimental ADF intensity of the stacking fault is compared with the intensity profiles from simulated data for the two main candidate sequences with the correct hexagonal symmetry: AA (1H), and β ($2H_c$).

(using the experimental parameters given at the beginning of this Supporting Information) were performed for the possible stacking sequences and the relative intensities compared to experimental data (Figure 8 and Figure S7). The red and blue colors in Figure S7 indicate intensity line scans comparing possible stacking sequences for the perfect parent crystal and in the stacking fault. For InSe the large mass difference between indium and selenium means that it is straight-forward to distinguish between the two candidate stacking configurations. The faults in Figures 8k and S6a are identified as consisting of a transition from γ to AA stacked regions, with γ being the expected, thermodynamically stable polytype and AA being obtained *via* a pure shear translation of (1/3) [-210]. The GaSe stacking fault data in Figure 8a is consistent with a similar structural translation; shifting from the most stable polytype (ε, top) to AA stacking (bottom). Although the experimental data for the stacking fault in GaSe is also consistent with the fault consisting of β-stacking, this would require antiparallel (180°) alignment of the crystal layers and hence a 60° rotation of the crystal lattice compared to the parent ε polytype. However, we consider this transition to be physically highly unlikely to have occurred for these large areas of crystal, even under the considerable stresses induced during mechanical exfoliation of the crystal.

References

(1)   Meyer, J. C.; Eder, F.; Kurasch, S.; Skakalova, V.; Kotakoski, J.; Park, H. J.; Roth, S.; Chuvilin, A.; Eyhusen, S.; Benner, G.; Krasheninnikov, A. V.; Kaiser, U. Erratum: Accurate Measurement of Electron Beam Induced Displacement Cross Sections for Single-Layer Graphene. *Phys. Rev. Lett.* **2013**, *110*, 239902.

(2)   Meyer, J. C.; Eder, F.; Kurasch, S.; Skakalova, V.; Kotakoski, J.; Park, H. J.; Roth, S.; Chuvilin, A.; Eyhusen, S.; Benner, G.; Krasheninnikov, A. V.; Kaiser, U. Accurate Measurement of Electron Beam Induced Displacement Cross Sections for Single-Layer Graphene. *Phys. Rev. Lett.* **2012**, *108*, 1–6.

(3)   McKinley, W. A.; Feshbach, H. The Coulomb Scattering of Relativistic Electrons by Nuclei. *Phys. Rev.* **1948**, *74*, 1759–1763.

(4)   Mott, N. F. The Scattering of Fast Electrons by Atomic Nuclei. *Proc. R. Soc. A Math. Phys. Eng. Sci.* **1929**, *124*, 425–442.

(5)   Komsa, H.-P.; Kotakoski, J.; Kurasch, S.; Lehtinen, O.; Kaiser, U.; Krasheninnikov, A. V. Two-Dimensional Transition Metal Dichalcogenides under Electron Irradiation: Defect Production and Doping. *Phys. Rev. Lett.* **2012**, *109*, 1–5.

(6)   Ho, C. Y.; Powell, R. W.; Liley, P. E. Thermal Conductivity of the Elements: A Comprehensive Review. *J. Phys. Chem. Ref. Data* **1974**, *3*, I1–I796.

(7)   Garcia, A.; Raya, A. M.; Mariscal, M. M.; Esparza, R.; Herrera, M.; Molina, S. I.; Scavello, G.; Galindo, P. L.; Jose-Yacaman, M.; Ponce, A. Analysis of Electron Beam Damage of Exfoliated MoS2 Sheets and Quantitative HAADF-STEM Imaging. *Ultramicroscopy* **2014**, *146*, 33–38.